Accurate Automated Detection of Autism Related Corpus Callosum Abnormalities

Ayman El-Baz, et al.

Journal of Medical Systems, 2011

NeuroSpectrum Insights, Inc.
info@neurospectruminsights.com
www.neurospectruminsights.com

J Med Syst (2011) 35:929–939
DOI 10.1007/s10916-010-9510-3

ORIGINAL PAPER

Accurate Automated Detection of Autism Related Corpus Callosum Abnormalities

Ayman El-Baz · Ahmed Elnakib · Manuel F. Casanova · Georgy Gimel'farb · Andrew E. Switala · Desha Jordan · Sabrina Rainey

Received: 12 February 2010 / Accepted: 16 March 2010 / Published online: 6 May 2010

Abstract The importance of accurate early diagnostics of autism that severely affects personal behavior and communication skills cannot be overstated. Neuropathological studies have revealed an abnormal anatomy of the Corpus Callosum (CC) in autistic brains. We propose a new approach to quantitative analysis of three-dimensional (3D) magnetic resonance images (MRI) of the brain that ensures a more accurate quantification of anatomical differences between the CC of autistic and normal subjects. It consists of three main processing steps: (i) segmenting the CC from a given 3D MRI using the learned CC shape and visual appearance; (ii) extracting a centerline of the CC; and (iii) cylindrical mapping of the CC surface for its comparative analysis. Our experiments revealed significant differences (at the 95% confidence level) between 17 normal and 17 autistic subjects in four anatomical divisions, i.e. splenium, rostrum, genu and body of their CCs.

Keywords Segmentation · Modeling · Autism · Corpus callosum

Introduction

Autistic Spectrum Disorder (ASD), or autism, is a complex neurological disability characterized by qualitative abnormalities in behavior and higher cognitive functions [1]. It typically appears during the first three years of life and impacts development of social interaction and communication skills. Each individual is affected differently at varying degrees, from milder forms in which intellectual ability is high but social interaction is low, to the most severe cases typified by unusual, self-injurious, and aggressive behaviors. The latter may persist throughout life and inflict a heavy burden on those who interact with autistic persons. Cognitive impairments may also last over time and often result in mental retardation in the majority of autistic individuals [2].

Autism is not a rare disorder, as once was thought. According to the Centers for Disease Control and Prevention (CDC), about 1 in 110 American children fall somewhere in the autistic spectrum. Although the cause of autism is still largely not clear, researchers have suggested that genetic, developmental, and environmental factors may be the cause or the predisposing effects towards developing autism [3]. No current cure is specifically designed for autism. However, educational, behavioral, or skill-oriented therapies were designed to remedy specific symptoms in each individual. Such therapies can result in substantial improvement, particularly when started at a young age.

Neuropathological and neuroimaging studies have revealed a great deal concerning the pathogenesis of autism. An overview of these studies as well as the proposed approach for analyzing MRI images of autistic and control subjects is illustrated below.

Neuropathology of autism

During the past two decades, the study of autism's neuropathology has dramatically intensified. Most studies have reported alterations in some regions of the brains in the autistic individuals compared to typically developing ones.

A. El-Baz (✉) · A. Elnakib · D. Jordan · S. Rainey
BioImaging Laboratory, Department of Bioengineering, University of Louisville, Louisville, KY, USA
e-mail: aselba01@louisville.edu

M. F. Casanova · A. E. Switala
Department of Psychiatry and Behavioral Science, University of Louisville, Louisville, KY, USA

G. Gimel'farb
Department of Computer Science, University of Auckland, Auckland, New Zealand

Increased head size was the first observed characteristic in children with autism 60 years ago [4]. Since then, several studies have reported enlarged brain size and head circumference (HC) in autistic patients. Postmortem studies have revealed evidence of increased brain weight, while bigger brain volume and macrocephaly, defined as HC above the 97th percentile [5]. Courchesne et al. [6] showed that while children with autism have an ordinary brain size at birth, they experience an acceleration of brain growth resulting, between 2 and 4 years of age, in increased brain volume relative to normal brains. By adolescence and adulthood, differences in the mean brain size between the two groups diminish largely because of increased relative growth in the control group; nonetheless, there exists an abnormal anatomy of cerebral white matter (CWM) in autistic brains [5, 6].

As an attempt to explain the pervasive symptomatology of autism, a recent neuropathological study theorized that the abnormalities in brain anatomy measured in the autistic brain are mainly due to altered distribution of minicolumns [7]. Minicolumns are the basic functional units of the brain that organizes neurons in cortical space [8, 9]. Investigators suggest that the cortex is made up of hundreds of millions of minicolumns [9, 10]. These units, having been found in all areas of the isocortex [11], derive from the radial glia unit that is present in all mammals [12]. Because of the large number of modules and their widespread distribution, abnormalities of the minicolumn's basic ontogenetic pattern may provide for macroscopic alterations. Therefore, it is not surprising that some of the gross changes observed in putative minicolumnopathies include variations in brain volume, in gyrification, and in the corpus callosum (CC) [7, 13, 14]. Recently, we have implemented an algorithm that measures the gyrification window and used it to derive a macroscopic neuropathological correlate to autism which relates to neuronal connectivity [14]. The size of the gyral window directly correlated to the size of the CC. A reduced gyral window constrains the possible size of projection fibers and biases connectivity towards shorter cortico-cortical fibers at the expense of longer association/commissural fibers. Based on these finding, we analyze the variability of the 3D CC surface in a group of autistic subjects and controls in order to quantify accurately how autism is associated with the abnormal neural development of the CC.

Image-analysis-based autism diagnostics

Multiple studies have identified different brain structures, e.g. grey matter, white matter, and CC structures, involved in abnormal neural development associated with autism. The image-analysis-based detection of such abnormalities is briefly overviewed below.

○ Grey matter

The grey matter is the brain cortex containing nerve cells and is responsible for routing sensory or motor stimuli to inter-neurons of the central nervous system. One hypothesizes the grey matter density in specific regions (regions thought to be involved in social recognition processes) of autistic brains is altered. Following this hypothesis, these brain regions were identified with a voxel-based morphometry (VBM) approach [15–18] using a freely available public domain software package (SPM [19]). The idea behind this approach is to normalize the brains stereotactically to a common space (e.g., an atlas with predefined anatomic subregions) and use voxel statistics to identify anatomic brain regions of altered grey matter density. Abel et al. [15] identified a decreased gray matter volume of the ASD group relative to the control group in the right paracingulate sulcus, the left inferior frontal gyrus, and an increased gray matter volume in amygdala and periamygdaloid cortex, middle temporal gyrus, inferior temporal gyrus, and in regions of the cerebellum. Boddaert et al. [18] found bilaterally significant decreases of grey matter concentration located in superior temporal sulcus comparing autistic children to normal children. Furthermore, a decrease of white matter concentration located in the right temporal pole and in the cerebellum was found in children with autism.

○ White matter

The white matter is responsible for connecting different areas of the gray matter within the nervous system. Several studies [20–23] attempted to identify how the connectivity (i.e. the white matter) between different gray matter areas is related to autism. Herbert et al. [20] applied a VBM approach and reported that boys ages 7–11 years with autism had a significantly larger volume of cerebral white matter (CWM) while cerebral cortex and hippocampus-amygdala had smaller volumes. Another VBM study [21] reported white matter volume deficits in the left middle temporal, right middle frontal, and left superior frontal gyri. Barnea-Goraly et al. [22] used Diffusion tensor imaging (DTI) to determine regions related to autism within the white matter. The DTI analysis derives important features of the brain tissue, e.g., fractional anisotropy (FA). The latter microstructural feature reflects how the diffusion within a voxel depends on orientation, i.e. specifies the degree of diffusion directionality. The study [22] reported reduced fractional anisotropy (FA) values in white matter adjacent to the ventromedial prefrontal cortices and in the anterior cingulate gyri as well as in the temporoparietal junctions. Additional clusters of reduced FA values were reported adjacent to the superior temporal sulcus bilaterally, in the temporal lobes approaching the amygdala bilaterally, in occipitotemporal tracts, and in the corpus callosum.

Our previous diagnostic system [23] attempted to quantify differences between the shape of CWM gyrifications for autistic and normal subjects using a three-step texture analysis of 3D MRI brain images. First, the CWM was segmented from a 3D MRI image using an evolving deformable boundary guided by both a probabilistic model of current visual appearance of the CWM and a learned prior appearance model. Then, the gyrifications were extracted from the segmented CWM, and their thickness was quantified in order to perform the classification.

- Corpus Callosum (CC)

The CC is the largest fiber bundle connecting the left and the right cerebral hemispheres in the human brain. Since the higher cognitive functions of the brain are highly affected by the impaired communication between the hemispheres, several studies [24–31] have proposed to analyze the CC for autistic subjects. In [24–27], the CC had been traced from the midsagittal MRI slice. Statistical difference analysis was applied to find out which part in the CC contributes significantly to identification of autistic brains. Chung et al. [28] applied a 2D VBM approach based on SPM software [19] to spatially normalize the midsagital MRI slice to a common stereotactic space in order to segment the CC and localize the CC subregions that are related to autism. To cover more CC anatomy, studies [29–31] account not only for the midsagital slice but also for four adjacent slices on both sides. He et al. [29] traced the CC from the nine slices based on a semi automated active contour methodology. A contour stitching technique was applied to create the 3D CC surfaces for each subject. Statistical difference analysis was applied to the signed distance map from each subject surface to a template. Instead of using a signed distance map metric, Vidal et al. [31] utilized the CC thickness—the distance between uniformly spaced points on the CC surface to the CC medial line (i.e., the average curve between superior and inferior CC boundaries)—to localize regions of callosal thinning in autism.

Our approach

To identify whether the abnormal neural development of the CC is associated with autism, we compare directly the 3D surfaces of the CC for normal and autistic subjects. To the best of our knowledge, all the previous works have focused on analyzing either the 2D cross section of the midsagittal of the CC or the midsagital slice along with four adjacent slices on both sides. Unfortunately, this is insufficient for detecting the whole anatomic variability of the CC of autistic subjects. To ensure a complete 3D analysis, the whole CC surface (traced from all the slices in which the CC appears) is mapped onto a cylinder in such a way as to compare more accurately various autistic and normal CCs. Our cylindrical mapping has been inspired by the functional conformal mapping [32]. Similar to the conformal mapping, it is a bijective (one-to-one) transformation and preserves angular relationships between the points. For these reasons, the conformal mapping was recently considered an efficient technique for surface matching [33] and visualization of various anatomic structures [34].

Methods

In this section, we will overview in brief our CC segmentation using a learned prior CC shape model and an identifiable joint Markov-Gibbs random field (MGRF) model of 3D MRI and 3D "object-background" region maps. Similar techniques have been already successful in segmenting various 2D MRI and CT objects (see e.g. [35, 36]), and the current algorithm has been modified to account for specific properties of the 3D CC. In this modification a 3D shape is described by a probabilistic model rather than a more conventional distance map. In addition, the centerline extraction for the segmented CC by solving the Eikonal equation is shown. In contrast to the known 2D solutions, e.g. in [35], the proposed process evolves in the 3D space in order to detect 3D points of the maximal curvature. Finally, the cylindrical mapping employed to evaluate the variability of the CC, after finding its centerline, is described.

Corpus callosum segmentation using a prior shape model

Let $\mathbf{Q} = \{0, 1, ..., Q-1\}$ be a set of Q integer grey levels and $\mathbf{L} = \{0,1\}$ be a set of object ("1") / background ("0") labels. A 3D grid $\mathbf{R} = \{(x,y,z) : x = 0, 1, ..., X-1; y = 0, 1, ..., Y-1; z = 0, 1, ...Z-1\}$ of voxels with integer Cartesian coordinates (x,y,z) supports grayscale MRI $\mathbf{g}:\mathbf{R}\rightarrow\mathbf{Q}$ and their region maps $\mathbf{m}:\mathbf{R}\rightarrow\mathbf{L}$. Let $P_s = \prod_{(x,y,z)\in\mathbf{R}} p_{x,y,z}$ be a prior probability distribution of co-registered CC shapes to be used for registering (aligning) the 3D MRI, $p_{x,y,z}$ being the voxel-wise object probability. Let a Gibbs distribution $P(\mathbf{m})$ specify a Markov-Gibbs random field (MGRF) model of the co-registered region maps. Let $P(\mathbf{g}|\mathbf{m}) = \prod_{(x,y,z)\in\mathbf{R}} p_{\mathbf{m}_{x,y,z}}\left(\mathbf{g}_{x,y,z}\right)$ be a conditionally independent distribution of the MRI signals, given the map. A joint distribution $P_s(\mathbf{g},\mathbf{m}) = P(\mathbf{g}|\mathbf{m})P(\mathbf{m})P_s$ specifies the MRGF model of the co-registered 3D MRI and their region maps.

As shown in Fig. 1, our objectives are to identify accurately a shape prior P_s for the co-aligned 3D MRI images, spatial label interactions in the model $P(\mathbf{m})$ of co-aligned region maps, and conditionally independent voxel-wise intensity distributions in the image model $P(\mathbf{g}|\mathbf{m})$. The shape prior P_s is learned from a training set of maps for manually

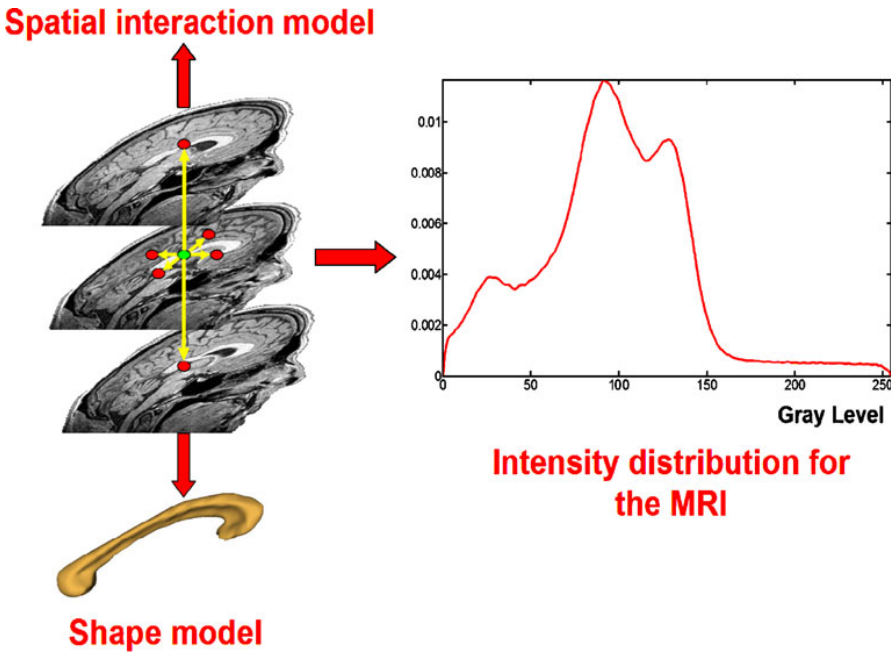

Fig. 1 Joint Markov-Gibbs random field model of 3D MR images

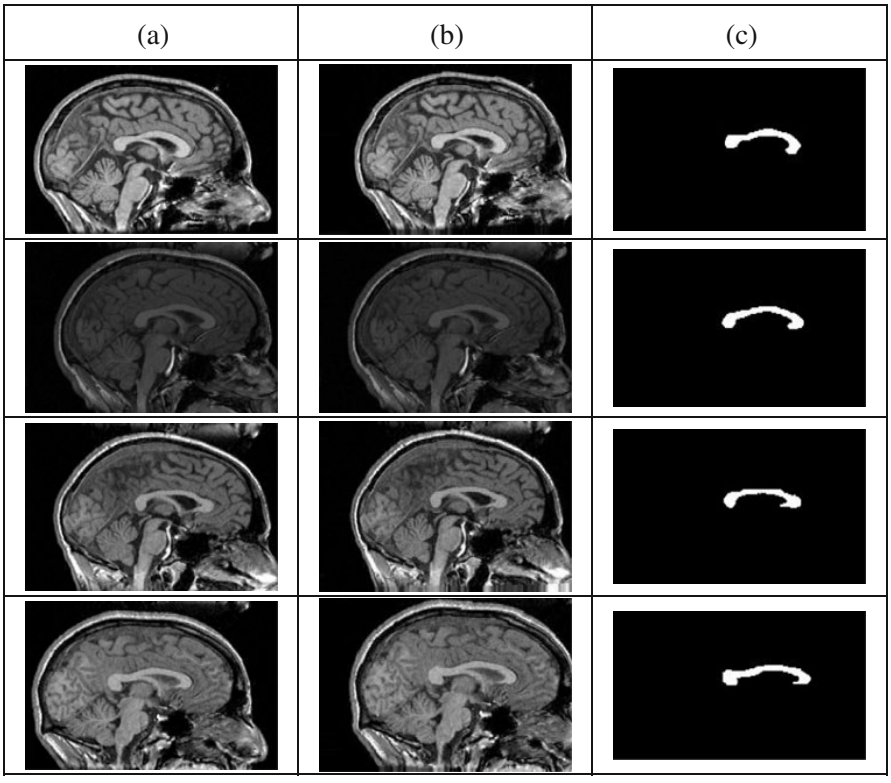

Fig. 2 Shape reconstruction (2D illustrations): database samples (**a**), affine mutual information based registration (**b**), and manual segmentation (**c**)

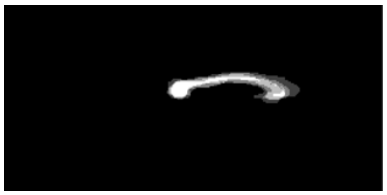

Fig. 3 Saggital cross-section in the estimated 3D voxel-wise probabilities of the CC shape

segmented and co-aligned images. To perform an initial CC segmentation, a given MRI image g is aligned to one of the training images. The shape prior $P_s = \prod_{(x,y,z)\in\mathbf{R}} p_{x,y,z}$ is used, together with the conditional image intensity model $P(\mathbf{g}|\mathbf{m})$, to build an initial region map $\mathbf{m}$. Then a joint MGRF model $P_s(\mathbf{g},\mathbf{m}) = P(\mathbf{g}|\mathbf{m})P(\mathbf{m})P_s$ identified from the 3D MRI $\mathbf{g}$ and its initial region map $\mathbf{m}$ is used for the final Bayesian segmentation.

○ Spatial voxel interaction in the CC

A generic MGRF of region maps in [37] accounts only for pairwise interaction between each region label and its characteristic neighbors. Generally, the interaction structure and the Gibbs potentials can be arbitrary and are identified from the training data. For simplicity, we restrict the interaction structure to the nearest voxels only (i.e. with the 26-voxel neighborhood). By symmetry considerations, we assume that the potentials are independent of relative orientation of each voxel pair and depend only on intra- or inter-region position (i.e. whether the labels are equal or not). Under these restrictions, it is the 3D extension of the conventional auto-binomial, or Potts model differing only in that the potentials are estimated analytically.

The 26-neighborhood has three types of symmetric pairwise interactions specified by the absolute distance a between

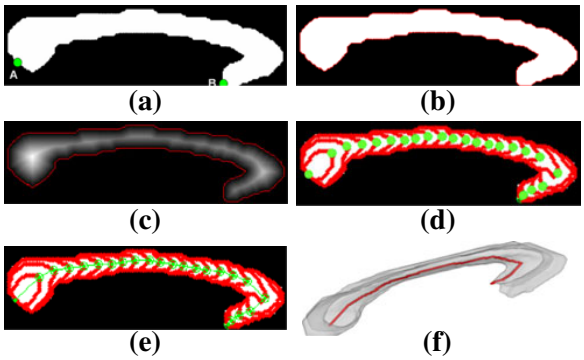

Fig. 4 Steps of the proposed centerline algorithm illustrated by the saggital 2D cross-sections of the 3D CC (**a**), estimated 3D CC edges (**b**), the normalized distance map (**c**), the orthogonal wave propagated from A (**d**), the extracted centerline (**e**), and its 3D visualization (**f**)

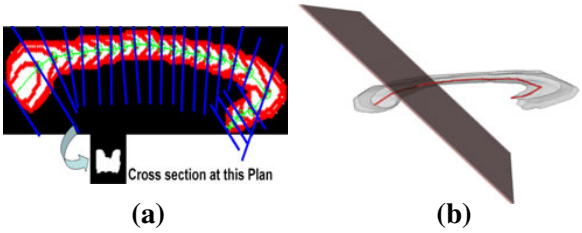

Fig. 5 2D (**a**) and 3D (**b**) illustrations of re-slicing

two voxels in the same and adjacent MRI slices ($a = 1, \sqrt{2}$, and $\sqrt{3}$, respectively): (i) the closest pairs with the inter-voxel $\mathbf{N}_1 = \{(1,0,0),(0,1,0),(0,0,1)\}$ coordinate offsets; (ii) the diagonal pairs with the offsets $\mathbf{N}_{\sqrt{2}} = \{(0,1,\pm1),(1,0,\pm1),(1,\pm1,0)\}$; and (iii) the farthest diagonal pairs with the offsets $\mathbf{N}_{\sqrt{3}} = \{(1,\pm1,\pm1)\}$. The Gibbs potentials of each type are bi-valued because only label coincidence is accounted for: $\mathbf{V}_a = \{V_{a,eq}; V_{a,ne}\}$ where $V_{a,eq} \equiv V_a(l,l')$ if $l = l'$ and $V_{a,ne} \equiv V_a(l,l')$ if $l \neq l'$; $a \in \mathbf{A} = \{1,\sqrt{2},\sqrt{3}\}$. Then the MGRF model of region maps is as follows:

$$P(\mathbf{m}) = \frac{1}{Z}\exp\sum_{(x,y,z)\in\mathbf{R}}\sum_{a\in\mathbf{A}}\sum_{(\xi,\eta,\kappa)\in\mathbf{N}} V_a\left(m_{x,y,z}, m_{x+\xi,y+\eta,z+\kappa}\right) \tag{1}$$

where Z is the normalizing factor (partition function).

To identify the MGRF in Eq. 1, approximate analytical maximum likelihood potential estimates are formed as follows[1]:

$$V_{a,eq} = -V_{a,ne} = 2\left(f_{a,eq}(\mathbf{m}) - \frac{1}{2}\right) \tag{2}$$

Here, $f_{a,eq}(\mathbf{m})$ denotes the relative frequency of the equal labels in the equivalent voxel pairs $\{((x,y,z),(x+\xi,y+\eta,z+\kappa)) : (x,y,z)\in\mathbf{R}; (x+\xi,y+\eta,z+\kappa)\in\mathbf{R}; (\xi,\eta,\kappa)\in\mathbf{N}_a\}$ of a region map $\mathbf{m}$ of a given MRI aligned in accord with the prior shape model.

○ Conditional intensity model for 3D MRI

Just as in [36, 38], a 3D MRI, given a region map, is modeled with a simple conditionally independent random field of voxel intensities: $P(\mathbf{g}|\mathbf{m}) = \prod_{(x,y,z)\in\mathbf{R}} p_{m_{x,y,z}}\left(\mathbf{g}_{x,y,z}\right)$ where the voxel-wise probability distributions $p_\lambda = [p_\lambda(q) : q\in\mathbf{Q}]$; $\lambda\in\mathbf{L}$, for the CC and its background are estimated during the segmentation. To separate p_0 and p_1, the mixed empirical distribution of all voxel intensities is closely approximated with a linear combination of discrete Gaussians (LCDG) with two dominant modes related to the object (i.e.

[1] To the best of our knowledge, we are the first authors who introduced an analytical form to estimate Gibbs potentials [36].

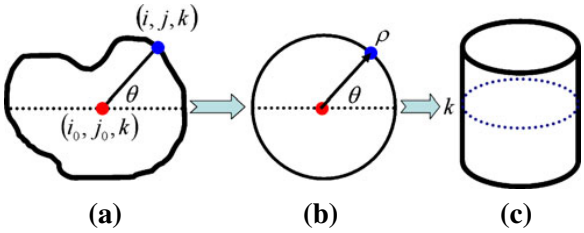

Fig. 6 Cylindrical mapping: a cross-section of the re-sliced CC (**a**), the CC cross-section mapped onto a circle (**b**), placing the circle onto the corresponding location in the cylinder (**c**)

the CC) and background, respectively. The LCDG including numbers of its positive and negative terms is obtained with our previous Expectation-Maximization-based algorithm introduced in [36, 38].

○ Prior CC shape model

Most of the recent works on image segmentation use level set based representations of shapes: an individual shape is outlined by a set of boundary pixels or voxels at the zero level of a certain signed distance function, and each given shape is approximated with the closest linear combination of the training shapes. The main drawback of this representation is that the space of distances is not closed with respect to linear operations. As a result, linear combinations of the distance functions may relate to invalid or even physically impossible boundaries.

To circumvent this limitation, the probabilistic 3D CC shape model $P_s = \prod_{(x,y,z)\in \mathbf{R}} p_{x,y,z}$ where $p_{x,y,z}$ is the empirical probability that the voxel (x,y,z) belongs to the CC is learned from the co-registered training MRI. Such a prior is constructed by co-aligning the training set of MRI by a rigid 3D registration using mutual information as similarity measure [39] (Fig. 2(a; b)); segmenting the CCs by hand from the aligned set (Fig. 2(c)), and counting how many times each voxel (x, y, z) was segmented as the CC (Fig. 3).

○ Segmentation algorithm

In total, the proposed CC segmentation process involves the following steps:

1. Affine alignment of a given 3D MRI to an arbitrary CC prototype from the training set using mutual information as similarity measure.
2. Estimating the conditional intensity model $P(\mathbf{g}|\mathbf{m})$ by identifying the bimodal LCDG.
3. Forming an initial region map m of the CC by using the found conditional intensity model and the learned prior shape model.
4. Identifying the MGRF model $P(\mathbf{m})$ from the initial map and updating the conditional intensity model $P(\mathbf{g}|\mathbf{m})$.
5. Final Bayesian CC segmentation using the updated joint MGRF model $P_s(\mathbf{g},\mathbf{m})$.

Centerline extraction from the CC

The problem of extracting the centerline connecting splenium (e.g. the point A in Fig. 4(a)) with rostrum (the point B) can be formulated as a minimum-cost problem: find the path that minimizes the cumulative cost of traveling from the starting point A to the destination B. As defined in [40], if $W(x, y, z)$ is a cost function at any location (x,y,z) inside the CC then the minimum cumulative cost at the location $B = (x', y', z')$ is

$$T(B) = \min_{C_{AB}} \int_0^L W(C(l))dl \tag{4}$$

where L is the path length and C_{AB} is a set of all possible paths linking A to B such that $C(0) = A$ and $C(L) = B$ are the starting and ending points of each path $C(l) \in C_{AB}$. The minimum cost path solving Eq. 4 also satisfies the solution of the Eikonal equation:

$$|\nabla T(x,y,z)|F(x,y,z) = 1 \tag{5}$$

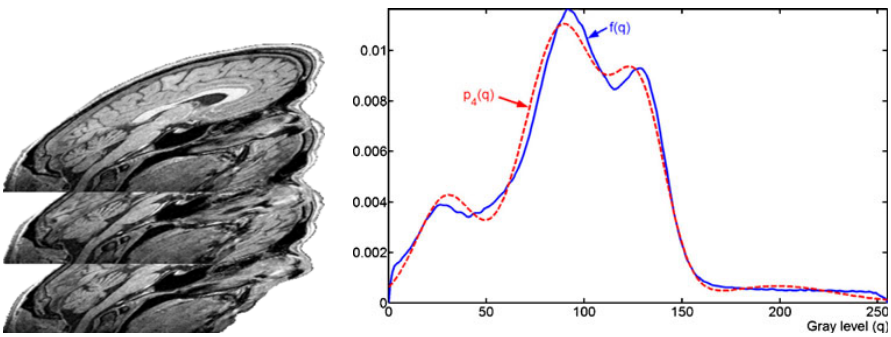

Fig. 7 Typical MRI slices (**a**) and the estimated density using four Gaussian components to represent each class in the brain images (**b**)

where $T(x, y, z)$ is the time at which the front evolving from the point A crosses the point (x,y,z) and $F(x, y, z)$is the speed function.

We propose a new algorithm to extract the centerline of the 3D CC based on solving Eq. 5:

1. Find the boundary of the segmented CC by estimating its 3D edges (see Fig. 4(b)).
2. Find the normalized minimum Euclidian distance $D(x, y, z)$ from every inner CC point (x,y,z) to the CC boundary (Fig. 4(c)) by solving Eq. 5 using the fast marching level sets at the unit speed function, $F(x, y, z) = 1$ [41].
3. Extract points located on the 3D centerline of the CC as follows:
   (a) Pick any splenium point as a starting point, A.
   (b) Propagate an orthogonal wave from the point A by solving Eq. 5 using the fast marching level sets at the speed function $F(x, y, z) = \exp(-D(x, y, z))$ (Fig. 4(d)).
   (c) Track the point with the maximum curvature as in [35, 42] and located at the maximum distance from the CC boundary for each propagating wave front (Fig. 4(e,f)), this point being considered at any time as corresponding to the starting point A.

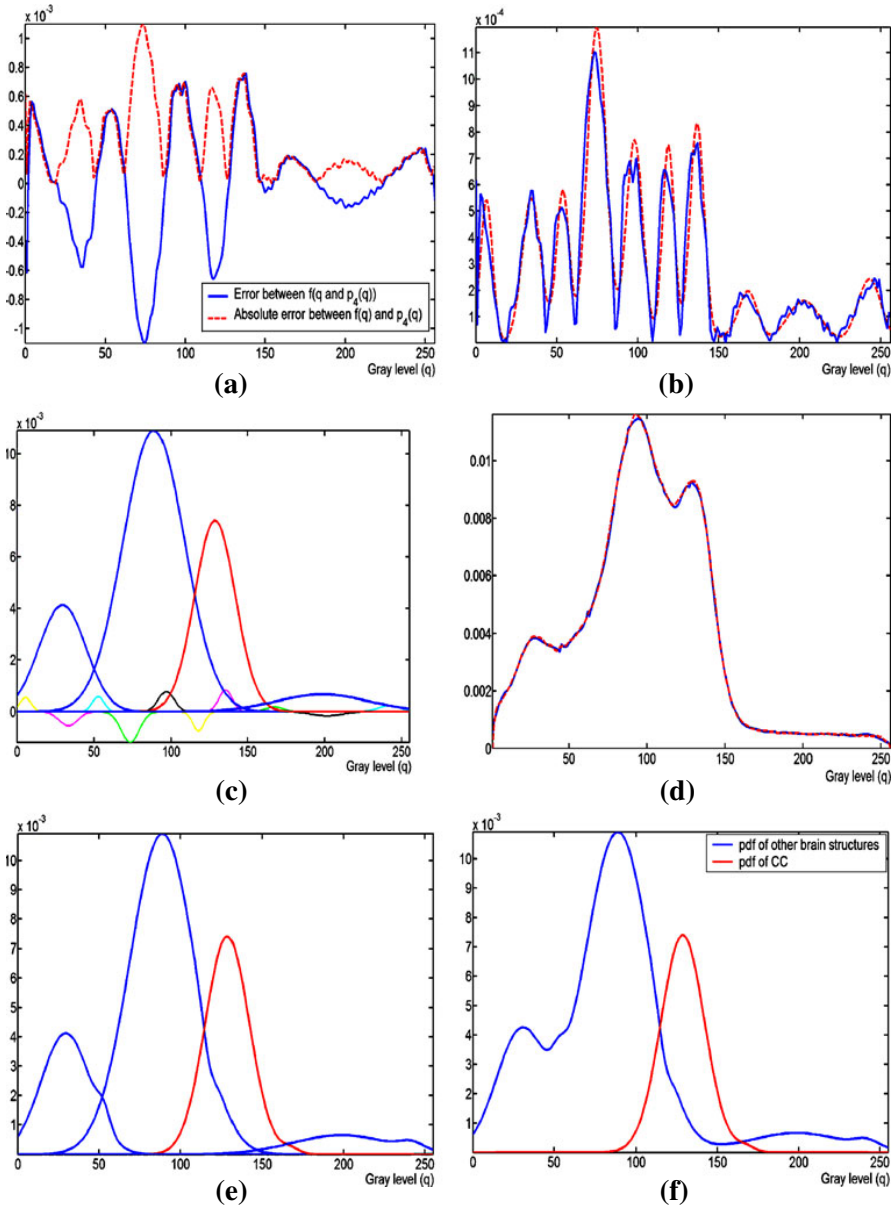

Fig. 8 Deviations and absolute deviations between $f(q)$ and $p_4(q)$ (**a**), estimated density of the absolute deviation (**b**), LCDG components (**c**), final estimated joint density (**d**), final estimated marginal density for each class (**e**), and final estimated marginal density for the CC and other brain structures (**f**)

(d) The point B at which the maximum curvature point of the propagating wave hits rostrum of the CC is selected as the end point of the centerline.

Cylindric mapping to evaluate CC variability

We reveal differences between the autistic and normal CC by using cylindric transformation. Before applying the cylindric transformation, the extracted 3D CC is re-sliced by generating planes that are orthogonal to and equidistant along the centerline as shown in Fig. 5(a,b). The re-slicing transforms 3D coordinates (x, y, z) of the voxels associated with each subsequent slice k into specific new coordinates (i, j, k) where (i, j) are 2D coordinates in the corresponding slicing plane k. A boundary point (i, j) of each slice k is related to the surface of a cylinder with a fixed radius ρ as shown in Fig. 6. The rectified centerline of the CC is superposed onto the cylinder axis. Polar coordinates (r, θ) of the boundary point (i, j, k) with respect to the slice center (i_0, j_0, k), being the trace of the centerline:

$$r = \sqrt{(i - i_0)^2 + (j - j_0)^2}; \theta = \tan^{-1}\left(\frac{j - j_0}{i - i_0}\right) \quad (6)$$

associate the point $(i, j, k) \equiv (r, \theta, k)$ with the point (ρ, θ, k) on the cylindrical surface. The resulting distribution of the radii r over this surface represents the segmented CC.

Results

The proposed approach has been tested on in-vivo data collected from 17 autistic subjects aged 16 to 22 years, and a group of 17 controls who match for gender, age, educational level, socioeconomic background, handedness, and general intelligence. All the subjects are physically healthy and free of history of neurological diseases and head injury. Briefly, all the subjects have exactly the same psychiatric conditions. All images were acquired with the same 1.5T MRI scanner (GE, Milwaukee, Wisconsin, USA) with voxel resolution $1.0 \times 1.0 \times 1.25$ mm^3 using a T1 weighted imaging sequence protocol. The "ground truth" diagnosis to evaluate the classification accuracy for each patient was given by clinicians.

A typical stack of MRI slices, its empirical marginal gray level distribution $f(q)$, and the initial 4-component Gaussian dominant mixture $p_4(q)$ are shown in Fig. 7. Figure 8 presents the steps of density estimation of the

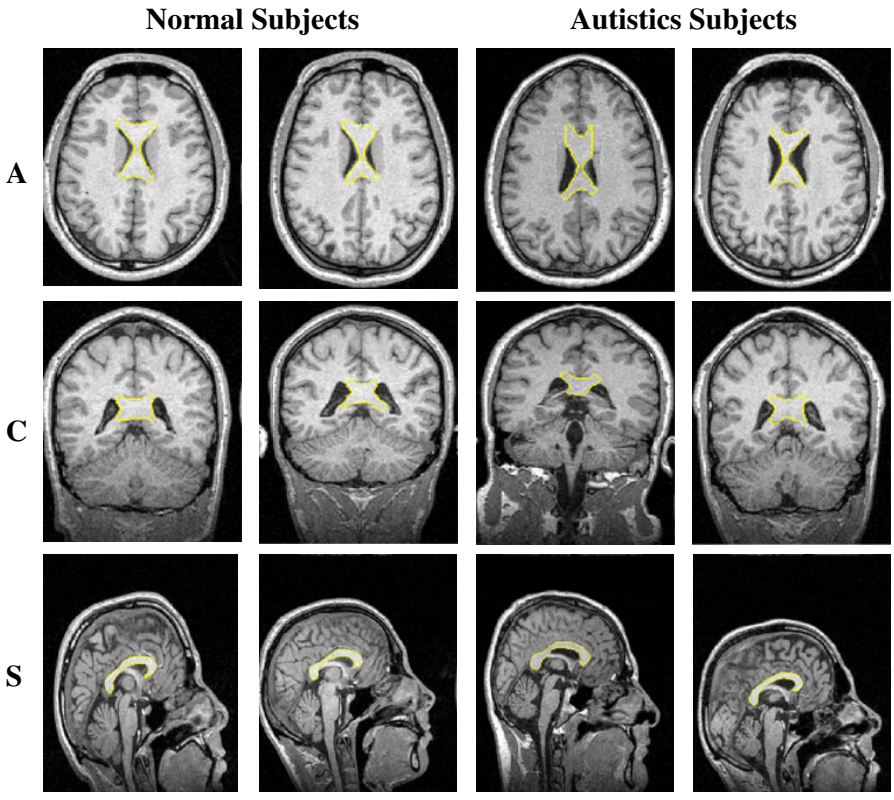

Fig. 9 Automated 3D CC segmentation results projected onto the 2D axial (*A*), coronal (*C*), and saggital (*S*) planes for visualization

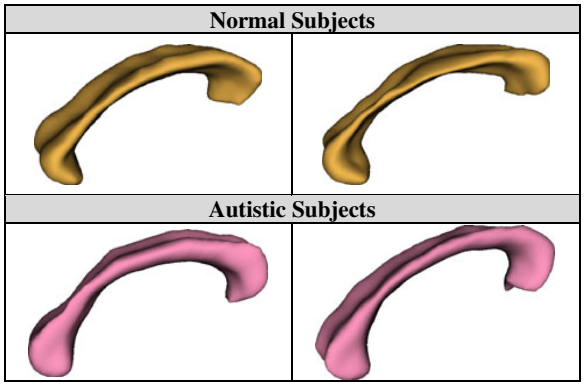

Fig. 10 3D CC of the normal and autistic subjects

LCDG-model using the modified EM-algorithm. The final LCDG of the CC and other brain structures are shown in Fig. 8(f). The CC segmentation is illustrated in Figs. 9, 10, and Table 1 shows comparative results for the 17 data sets which are not used in the training with the known ground truth (manually segmented by an expert). The differences in the mean errors between the proposed segmentation, the level-set shape based approach of Tsai et al. [34], and ASM segmentation [44] are statistically significant according to the unpaired *t*-test (the two-tailed value *P* is less than 0.0001).

Figures 11(a) and (b) present the average cylindrical maps for 17 normal subjects and 17 autistic subjects. As shown in Fig. 11(c), some locations in these maps differ significantly for the normal and autistic subjects at the 95% confidence level. The inverse cylindrical mapping outlines the significant areas on the average CC of normal subjects as shown in Fig. 12. These areas show that these significant differences (at the 95% confidence interval) exist in the four anatomical divisions of the CC, namely, splenium, rostrum, genu, and body. Fig. 12 demonstrates that the CC body for the autistic subjects is thinner than for the normal ones.

Table 1 Accuracy on 17 data sets of our segmentation comparing to the level sets based segmentation [43] and the active shape model (ASM) segmentation [44]

	Algorithm		
	Our	[43]	[44]
Minimum error, %	**0.17**	6.70	10.50
Maximum error, %	**2.15**	14.10	23.30
Mean error, %	**1.30**	9.70	13.98
Standard deviation, %	**1.70**	3.30	7.10
Significant difference, P-value		0.0001	0.0001

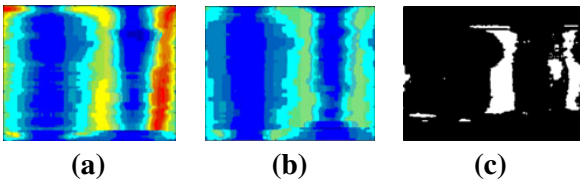

Fig. 11 Average cylindrical maps of the normal (**a**) and autistic (**b**) subjects and areas (**c**) of the 95%-significant difference between the normal and autistic subjects

Discussion

The reduction of the body of the CC of autistic subjects that is demonstrated in this paper is perfectly correlated with the Meta-Analysis study which was done by Frazier et al. [45]. Frazier et al. made a statistical analysis for the results of 10 studies (from 1987 to 2007) with contributed data from 253 patients with autism and 250 healthy control subjects [24–27, 31, 46–50]. Moreover, the proposed 3D mapping approach has the capability to demonstrate the whole anatomical differences (voxel-based) between CC of normal and autistic brains instead of only differences in the CC divisions (area-based) as done with the previous groups [24–27, 31, 46–50]. Thus, the existing differences in all anatomical divisions of the CC, namely, splenium, rostrum, genu and body were identified as shown in Fig. 12.

Conclusion

In total, our preliminary results suggest that the proposed approach can detect significant differences in the four

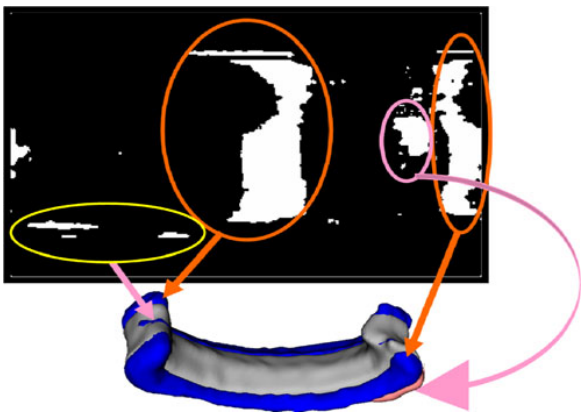

Fig. 12 Color-coded anatomical differences between the CC for normal and autistic subjects: the common parts (gray), parts existing for normal but not for autistic subjects (blue), and parts existing for autistic but not for normal subjects (pink)

anatomical divisions of the CC. Moreover, it has the ability to demonstrate the voxel-based anatomical differences between CC of normal and autistic brains instead of only area-based as done with the previous groups. In our future work, different brain structures will be investigated in order to quantitatively characterize the development and temporal changes of an autistic brain in order to achieve our ultimate goal for developing an efficient non-invasive computer-assisted system for early diagnosis of autism.

References

1. Brambilla, P., Hardan, A., and Nemi, S., Brain anatomy and development in autism: Review of MRI studies. *Brain Res. Bull.* 61:557–569, 2003.
2. Minshew, N., and Payton, J., New perspectives in autism, part i. the clinical spectrum of autism. *Curr. Probl. Pediatr.* 18:561–610, 1988.
3. Stevens, M., Fein, D., Dunn, M., Allen, D., Waterhouse, L. H., Feinstein, C., and Rapin, I., Subgroups of children with autism by cluster analysis: A longitudinal examination. *J. Am. Acad. Child Adolesc. Psychiatry* 39:346–352, 2000.
4. Kanner, L., Autistic disturbances of affective contact. *Nerv. Child* 2:250–250, 1943.
5. Aylward, E., Minshew, N., Field, K., Sparks, B., and Singh, N., Effects of age on brain volume and head circumference in autism. *Neurology* 59(2):175–183, 2002.
6. Courchesne, R., Carper, R., and Akshoomoff, N., Evidence of brain overgrowth in the first year of life in autism. *JAMA* 290:337–344, 2003.
7. Casanova, M. F., White matter volume increases and minicolumns in autism. *Ann. Neurol.* 56(3):453, 2004.
8. Casanova, M. F., van Kooten, I. A., Switala, A., van Engeland, H., Heinsen, H., Steinbusch, H., Hof, P. R., Trippe, J., Stone, J., and Schmitz, C., Minicolumnar abnormalities in autism. *Acta Neuropathological*, 2006.
9. Mountcastle, V. B., *Perpetual Neuroscience: The Cerebral Cortex*. Harvard University Press, Cambridge, 1988.
10. Calvin, W., *How Brains Think*. Basic Books, New York, 1996.
11. Buxhoeveden, D., and Casanova, M. F., Encephalization, minicolumns, and hominid evolution. In: Casanova, M. F. (Ed.), *Neocortical Modularity and the Cell Minicolumn*. Nova Biomedical, New York, pp. 117–136, 2005.
12. Gressens, P., and Evrard, P., The glial fascicle: An ontogenic and phylogenic unit guiding, supplying and distributing mammalian cortical neurons. *Brain Res. Dev. Brain Res.* 76:272–277, 1993.
13. Fahmi, R., El-Baz, A., Hassan, H., Farag, A., and Casanova, M. F., Classification Techniques for Autistic Vs. Typically Developing Brain Using MRI Data. *Proc. of IEEE International Symposium on Biomedical Imaging: From Nano to Macro (ISBI'07), Arlington, Virginia, USA* 1348–1351, 2007.
14. Casanova, M. F., Farag, A., El-Baz, A., Mott, M., Hassan, H., Fahmi, R., and Switala, A. E., Abnormalities of the gyral window in autism: A macroscopic correlate to a putative minicolumnopathy. *J. Spec. Educ. Rehabil.* 1:85–101, 2007.
15. Abell, F., Krams, M., Ashburner, J., Passingham, R., Friston, K., Frackowiak, R., Happe, F., Frith, C., and Frith, U., The neuroanatomy of autism: A voxel-based whole brain analysis of structural scans. *NeuroReport* 10(8):647–1651, 1999.
16. Waiter, G., Williams, J., Murray, A., Gilchrist, A., Perrett, D., and Whiten, A., A voxel-based investigation of brain structure in male adolescents with autistic spectrum disorder. *Neuroimage* 22:619–625, 2004.
17. Rojas, D. C., Peterson, E., Winterrowd, E., Reite, M. L., Rogers, S. J., and Tregellas, J. R., Regional gray matter volumetric changes in autism associated with social and repetitive behavior symptoms. *BMC Psychiatry* 6(56), 2006.
18. Boddaert, N., Chabane, N., Gervais, H., Good, C. D., Bourgeois, M., Plumet, M. H., Barthelemy, C., Mouren, M. C., Artiges, E., Samson, Y., Brunelle, F., Frackowiak, R. S. J., and Zilbovicius, M., Superior temporal sulcus anatomical abnormalities in childhood autism: a voxel-based morphometry MRI study. *Neuroimage* 23:364–369, 2004.
19. *Statistical Parametric Mapping* (*SPM*) *Software*, available online: http://www.fil.ion.ucl.ac.uk/spm/
20. Herbert, M. R., Ziegler, D. A., Deutsch, C. K., O'Brien, L. M., Lange, N., Bakardjiev, A., Hodgson, J., Adrien, K. T., Steele, S., Makris, N., Kennedy, D., Harris, G. J., and Caviness, V. S., Jr., Dissociations of cerebral cortex, subcortical and cerebral white matter volumes in autistic boys. *Brain* 126:1182–1192, 2003.
21. Waiter, G. D., Williams, J. H., Murray, A. D., Gilchrist, A., Perrett, D. I., and Whiten, A., Structural white matter deficits in high-functioning individuals with autistic spectrum disorder: A voxel-based investigation. *Neuroimage* 24(2):455–461, 2005.
22. Barnea-Goraly, N., Kwon, H., Menon, V., Eliez, S., Lotspeich, L., and Reiss, A. L., White matter structure in autism: Preliminary evidence from diffusion tensor imaging. *Biol. Psychiatry* 55:323–328, 2004.
23. El-Baz, A., Casanova, M. F., Gimel'farb, G., Mott, M., and Switala, A. E., Autism Diagnostics by 3D Texture Analysis of Cerebral White Matter Gyrifications. *Proc. of International Conference on Medical Image Computing and Computer-Assisted Intervention (MICCAI'07), Brisbane, Australia* 235–243, 2007.
24. Egaas, B., Courchesne, E., and Saitoh, O., Reduced size of corpus callosum in autism. *Arch. Neurol.* 52(8):794–801, 1995.
25. Piven, J., Bailey, J., Ranson, B. J., and Arndt, S., An MRI study of the corpus callosum in autism. *Am. J. Psychiatry* 154(8):1051–1056, 1997.
26. Manes, F., Piven, J., Vrancic, D., Nanclares, V., Plebst, C., and Starkstein, S., An MRI study of the corpus callosum and cerebellum in mentally retarded autistic individuals. *J. Neuropsychiatry Clin. Neurosci.* 11(4):470–474, 1999.
27. Hardan, A. Y., Minshew, N. J., and Keshavan, M. S., Corpus callosum size in autism. *Neurology* 55:1033–1036, 2000.
28. Chung, M. K., Dalton, K. M., Alexander, A. L., and Davidson, R. J., Less white matter concentration in autism: 2D voxel-based morphometry. *Neuroimage* 23:242–251, 2004.
29. He, Q., Duan, Y., Miles, J., and Takahashi, N., Statistical Shape Analysis of the Corpus Callosum in Subtypes of Autism, *Proc. 7th IEEE Int. Conf. BIBE* 1087–1091, 2007.
30. He, Q., Karsch, K., and Duan, Y., Abnormalities in MRI traits of Corpus Callosum in Autism Subtype. in *Proc. 30th IEEE Int. Conf. of EMBS* pp. 3900–3903, 2008.
31. Vidal, C. N., Nicolson, R., DeVito, T. J., Hayashi, K. M., Geaga, J. A., Drost, D. J., Williamson, P. C., Rajakumar, N., Sui, Y., Dutton, R. A., Toga, A. W., and Thompson, P. M., Mapping corpus callosum deficits in autism: An index of aberrant cortical connectivity. *Biol. Psychiatry* 60(3):218–225, 2006.
32. Schinzinger, R., Conformal Mapping: Methods and Applications, Courier Dover Publications, 2003.
33. Wang, S., Wang, Y., Jin, M., Gu, X., and Samaras, D., Conformal geometry and its applications on 3D shape matching, recognition and stitching. *IEEE Trans. Pattern Anal. Mach. Intell.* 29 (7):1029–1220, 2007.
34. Hong, W., Gu, X., Qiu, F., Jin, M., and Kaufman, A., Conformal virtual colon flattening. *Proc. ACM Symp. Solid and Physical Modeling, Wales, UK*:85–93, 2006.

35. El-Baz, A., and Gimel'farb G., Image segmentation with a parametric deformable model using shape and appearance priors, *Proc. IEEE Conf. Computer Vision and Pattern Recognition, Anchorage, AL, USA* pp. 1–8, 2008.
36. Farag, A., El-Baz, A., and Gimel'farb, G., Precise segmentation of multi-modal images. *IEEE Trans. Image Process.* 15(4):952–968, 2006.
37. Gimel'farb, G., *Image Textures and Gibbs Random Fields*. Kluwer Academic, Dordrecht, 1999.
38. El-Baz, A., and Gimel'farb, G., EM based approximation of empirical distributions with linear combinations of discrete Gaussians. *Proc. IEEE Int. Conference on Image Processing, San Antonio, Texas, USA* 4:373–376, 2007.
39. Viola, P., and Wells, W. M., Alignment by maximization of mutual information. *Proc. 5th Int. Conference on Computer Vision*16–23, 1995.
40. Cohen, L., and Kimmel, R., Global minimum for active contour models: A minimal path approach. *Int. J. Comput. Vis.* 24(1):57–78, 1997.
41. Adalsteinsson, D., and Sethian, J., A fast level set method for propagating interfaces. *J. Comput. Phys.* 118(2):269–277, 1995.
42. Hassouna, M., and Farag, A., Robust Centerline Extraction Framework Using Level Sets, *Proc. of IEEE Conference on Computer Vision and Pattern Recognition (CVPR), San Diego, CA, USA* 458–465, 2005.
43. Tsai, A., Yezzi, A., Wells, W., Tempany, C., Tucker, D., Fan, A., Grimson, W. E., and Willsky, A., A shape based approach to the segmentation of medical imagery using level sets. *IEEE Trans. Med. Imaging* 22:137–154, 2003.
44. Cootes, T., and Taylor, C., A mixture model for representing shape variation. *Image Vis. Comput.* 17(8):567–574, 1999.
45. Frazier, T. W., and Harden, Y. H., A meta-analysis of the corpus callosum in Autism. *Biol. Psychiatry* 66(10):935–941, 2009. Nov 15.
46. Just, M. A., Cherkassky, V. L., Keller, T. A., Kana, R. K., and Minshew, N. J., Functional and anatomical cortical underconnectivity in autism: Evidence from an fMRI study of an executive function task and corpus callosum morphometry. *Cereb. Cortex* 17:951–961, 2007.
47. Boger-Megiddo, I., Shaw, D. W., Friedman, S. D., Sparks, B. F., Artru, A. A., Giedd, J. N., Dawson, G., and Dager, S. R., Corpus callosum morphometrics in young children with autism spectrum disorder. *J. Autism Dev. Disord.* 36:733–739, 2006.
48. Rice, S. A., Bigler, E. D., Cleavinger, H. B., Tate, J., Sayer, D. F., McMahon, W., Ozonoff, S., Lu, J., and Lainhart, J. E., Macrocephaly, corpus callosum morphology, and autism. *J. Child Neurol.* 20:34–41, 2005.
49. Elia, M., Ferri, R., Musumeci, S. A., Panerai, S., Bottitta, M., and Scuderi, C., Clinical correlates of brain morphometric features of subjects with low-functioning autistic disorder. *J. Child Neurol.* 15:504–508, 2000.
50. Gaffney, G. R., Kuperman, S., Tsai, L. Y., Minchin, S., and Hassanein, K. M., Midsaggital magnetic resonance imaging of autism. *Br. J. Psychiatry* 151:831–833, 1987.